



Generation of broadband correlated photon-pairs in short thin-film lithium-niobate waveguides

BRADLEY S. ELKUS,^{1,*}  KAMAL ABDELSALAM,²  ASHUTOSH RAO,^{2,3}  VESSELIN VELEV,^{1,4}  SASAN FATHPOUR,²  PREM KUMAR,¹  AND GREGORY S. KANTER¹

¹Department of Electrical and Computer Engineering, Center for Photonic Communication and Computing, Northwestern University, 2145 Sheridan Road, Evanston, Illinois 60208-3118, USA

²CREOL, The College of Optics and Photonics, University of Central Florida, Orlando, Florida 32816, USA

³Currently with the Microsystems and Nanotechnology Division, Physical Measurement Laboratory, National Institute of Standards and Technology, Gaithersburg, Maryland 20899, USA, and the University of Maryland, College Park, Maryland 20742, USA

⁴Currently with Elenion Technologies, 171 Madison Ave #1100, New York, NY 10016, USA

*bradleyelkus2013@u.northwestern.edu

Abstract: An efficient source of quantum-correlated photon-pairs that is integrable with existing silicon-electronics fabrication techniques is desirable for use in quantum photonic integrated circuits. Here we demonstrate signal-idler photon pairs with high coincidence-to-accidental count ratios of over 10^3 on a coarse wavelength-division-multiplexing grid that spans 140 nm by using a 300- μm -long poled region in a thin-film periodically-poled lithium-niobate ridge waveguide bonded to silicon. The pairs are generated via spontaneous parametric downconversion pumped by a continuous-wave tunable laser source. The small mode area of the waveguide allows for efficient interaction in a short length of the waveguide and, as a result, permits photon-pair generation over a broad range of signal-idler wavelengths.

© 2019 Optical Society of America under the terms of the [OSA Open Access Publishing Agreement](#)

1. Introduction

A source of bright, wideband, quantum-correlated photon-pairs integrated on a silicon chip is useful for deployment in quantum photonic integrated circuits (PICs). Ideally, such a source can be integrated with other PIC devices, such as electro-optic (EO) switches, modulators, and optical filters [1–3], while remaining compatible with existing fabrication techniques used in silicon electronics. Although lithium niobate (LN) has excellent nonlinear and electro-optic properties, the generally large component sizes make PIC implementations problematic when attempting to fit many devices on a single chip. Traditional lithium-niobate technology typically requires cm-scale waveguides [4] for photon-pair generation and EO switching. Such sizes reduce the potential for integration, while also constraining the bandwidth of the generated photon-pairs.

Thin-film LN (TFLN) is a modern technology platform capable of tighter integration of nonlinear devices that can be exploited for making brighter entangled photon-pair sources with shorter-length devices, while permitting wider phase-matching bandwidths. The increased nonlinear conversion efficiency stemming from the smaller waveguide dimensions shown in Fig. 1 can allow for a shorter interaction length [1,5–8] compared to reverse proton exchange (RPE) waveguides. RPE waveguides in the buried configuration have limitations on the amount of lateral confinement that can be created in the standard proton exchange process because of restrictions on the control of the index contrast between the waveguiding strips and surrounding lithium niobate. These RPE waveguides can have small-signal second-harmonic-generation

(SHG) conversion efficiencies η_{SHG} of around $150\% \text{ W}^{-1} \text{ cm}^{-2}$ [9]. In contrast to the above, TFLN can use either direct etching of the thin-film lithium niobate or rib-loading with index-matched materials to create the smaller lateral optical confinement. Most recently, direct-etched TFLN ridge structures wafer-bonded to SiO_2 have achieved η_{SHG} as high as $4600\% \text{ W}^{-1} \text{ cm}^{-2}$ [8].

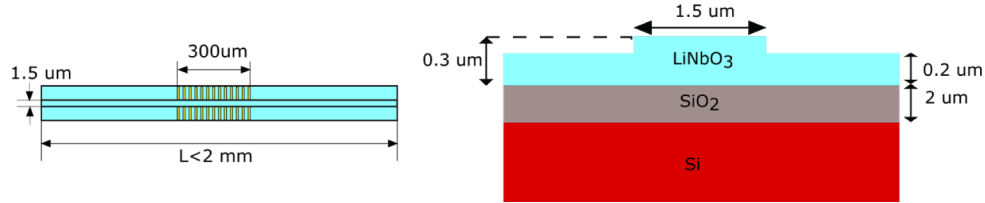


Fig. 1. Waveguide chip schematic of top view and cross-section: (a) Top view of waveguide where the waveguide length is less than 2 mm, and the poled region has total length of 300 μm . Opposing poling electrodes colored in yellow are separated by 8 μm and do not touch the waveguide of 1.5 μm in width. (b) The waveguide cross-section is $1.5 \times 0.3 \mu\text{m}^2$ composed of x-cut lithium niobate.

Both rib-loaded and direct-etched TFLN can be used for photon-pair generation [6,10] in short devices. Recently in [6], a 4-mm-long TFLN waveguide reported multiplexed pair generation with channel-center separations limited by the available filters to 6.9 nm. Photon-pair correlations over broader spectral ranges and channel-separations have been performed in other platforms ranging from fibers to resonators. For example, pair-sources from an induced second-order nonlinearity in periodically-poled silica fiber have been recently reported in a poled-fiber length of 20 cm, and produce a bi-photon spectrum of 100 nm [11]. While such a fiber source is not integrable, other technologies like SiN ring resonators [12] and LN microdisk resonators are compatible with dense PICs. LN microdisk resonators have been fabricated on silica pedestals, and can generate combs with large pair-matching bandwidths. A high-Q LN microresonator with 45 μm radius has shown measured correlations between signal-idler channels spanning about 100 nm, and based on spectrum measurements of the signal counts there is potentially up to 400 nm of available pair-matching bandwidth [13]. The generated spectrum of the signal-idler pairs in disk resonators is discrete because of the resonance condition imposed on the allowed modes. Unlike a disk resonator, the traveling wave structure in our periodically-poled lithium-niobate (PPLN) waveguide supports a continuous wideband spectrum of signal-idler pairs that can be sliced into different channels using standard filtering technology.

Here, we take a step towards photonic integration by realizing photon-pairs on a 20 nm coarse wavelength division multiplexed (CWDM) grid with channel-center separations up to 140 nm in TFLN. The sub-micron mode size achievable in this technology platform allows for a substantial reduction in the size of nonlinear and electro-optic devices, potentially enabling much denser PIC implementations. This work expands upon materials published in *Frontiers in Optics* [14].

2. Correlated photon-pair measurement scheme

2.1. PPLN nonlinear conversion efficiency

In our experiment, we generate photon-pairs via spontaneous parametric downconversion (SPDC) in the 300- μm -long poled region of a 1.5 mm-long ridge waveguide fabricated on TFLN bonded to silicon. The fabrication details of this device (structure shown in Fig. 1) can be found in [8]. Photon-pairs can be generated with a few μW or less of power in periodically poled waveguides when pumping at the second harmonic (SH) wavelength that would be generated under phase-matched SHG [15], which is about 771 nm in our present work. The SH small-signal conversion efficiency (undepleted-pump approximation [16]) is measured using the experimental

system depicted in Fig. 2 by tuning a CW pump from a Santec tunable laser (TSL-210) and using a fiber polarization controller (FPC) to excite the TE mode of the waveguide. The pump is split by a 99/1 splitter, monitored by a power meter, and coupled into (collected out of) the waveguide using lensed fiber (single mode at 1550 nm). The output pump and second harmonic are collected simultaneously by the same lensed fiber, separated by a 775/1550 nm band wavelength division multiplexer (BWDM) filter, and detected by power meters with real-time simultaneous monitoring of the pump insertion loss and SHG power. The measured SH small-signal conversion efficiency η_{SHG} is shown in Fig. 3(a) with a nearly 15-nm-wide phase-matching bandwidth centered around 1541 nm for the pump fundamental wavelength. The reported η_{SHG} is based on the estimated light intensities just before the output facet of the waveguide with facet-to-lensed fiber coupling losses of around 6.5 dB and less than 5 dB for the SH and fundamental pump at the phase-matching peak, respectively. The SH conversion efficiency (η_{SHG}) shown in Eq. (1) corrects for losses using the fundamental pump transmissivity G_f and the SH transmissivity G_{sh} , and includes the SH powers at the fundamental P_f and harmonic P_{sh} with total length of the poled region (L_p) in cm.

$$\eta_{SHG} = \frac{P_{sh}G_{sh}}{(P_fG_fL_p)^2} \times 100\% \quad (1)$$

The waveguide has flat polished endfaces which result in modest Fabry Perot resonances of both the pump-loss (Fig. 3(c)) and SH-loss. These resonances lead to the oscillations in the small signal conversion efficiency near the phase-matching peak in Fig. 3(a) that diminish for greater phase-mismatch (Fig. 3(b)). The data points are outlined in blue to highlight the oscillations at the phase-matching peak and the less obvious interference effects far from phase matching in Figs. 3(b) and (c). The corresponding peak conversion efficiency for down conversion will occur for signal/idler filters spaced symmetrically about 1541 nm in frequency space for a down-conversion pump around 771 nm.

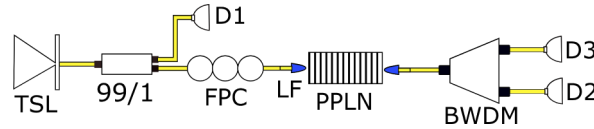


Fig. 2. Upconversion setup for SH phase-matching curve acquisition using a TSL:tunable Santec laser as a pump, FPC: fiber polarization controller, 99/1 splitter, 3 power meters (D1,D2,D3), LF:lensed fiber , 775/1550 nm BWDM.

Our down-conversion pump laser (Velocity 6300 by New Focus) can be tuned from 772.2 nm to longer wavelengths, making our optimal pump wavelength of 771 nm unreachable, but still within the SH phase-matching bandwidth. This results in a modest loss of efficiency, which is further compounded by the fact that when pumping at 772.2 nm the half-frequency of the down-conversion pump (1544.4 nm), hereinafter referred to as half-frequency pump ($f_p/2$), is not perfectly centered with respect to the signal and idler channel pairs (e.g. 1550 nm for 1530/1570 nm) of the 8-channel coarse-wavelength division multiplexing (CWDM) grid. Even though the CWDM grid has equal spacing between channel centers in wavelength, they are unequal in frequency space. This becomes more important for signal/idler channels sitting at very (non-energy conserving) unequal distances from the half-frequency pump. This nuance will require defining an effective bandwidth that is expected to contribute to correlations when looking at the many signal/idler wide-band channel sets considered in this work.

2.2. Pair generation setup with assymetric filter spacing

We measure correlations between a set of 4-signal/4-idler channels for signal/idler channel-centers ranging from (1470 to 1530 nm) and (1550 to 1610 nm). Our set-up, shown in Fig. 4, uses a

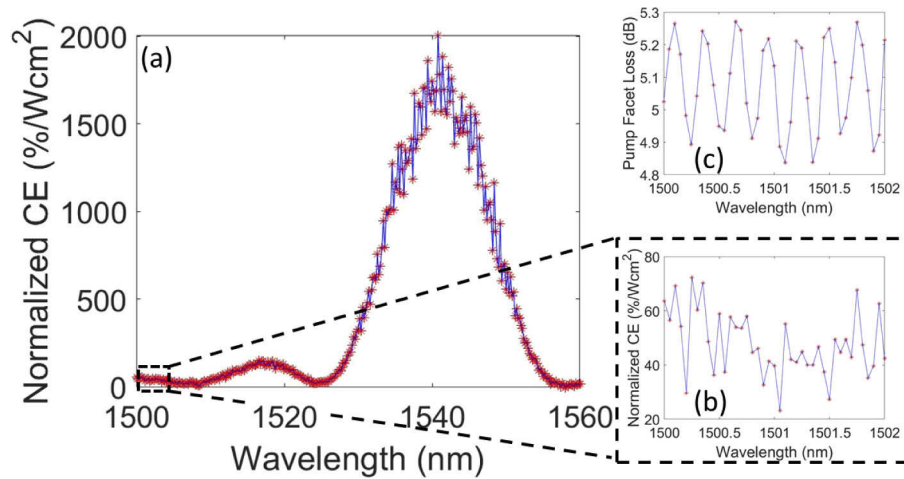


Fig. 3. (a) Phase matching curve of η_{SHG} (resonances outlined in blue) assuming a SH facet-to-lensed fiber coupling loss of 6.5 dB out from the waveguide facet to the collection-lensed fiber. (b) η_{SHG} measured far from phase matching (c) up-conversion pump facet-to-lensed fiber coupling loss (resonances outlined in blue) used in calculation of (b).

series of waveplates to control the pump power and polarization launched into the waveguide. A tap is inserted before the waveguide to monitor the pump wavelength, but not relied on for insertion loss measurements of the down-conversion pump power. The pump is coupled into (out of) the waveguide via a lensed fiber that is single mode (SM) at 780 nm (1550 nm). Emerging from the waveguide, the SPDC pairs are separated from the pump using a combination of fiber (775/1550 BWDM) and free-space filters (short-pass Dichroic) that provide ≥ 110 dB of pump isolation prior to additional pump filtering provided by the 8-channel CWDM demultiplexer. A power meter is used to monitor the power out of the waveguide via the 775- BWDM port. For the fundamental wavelength we estimate the waveguide output coupling loss into the collection-lensed fiber to be around 4 dB for the entire 120 nm range of interest. This loss is inferred from half the total insertion loss from lensed-fiber to lensed-fiber (both SM at 1550 nm and anti-reflection coated) using a polarized-broadband ASE source from a semiconducting optical amplifier, and measuring both the input and output spectrum on an optical spectrum analyzer (OSA). Half the measured insertion loss of the down-conversion pump can be between 6 and 7.5 dB depending on the angle between the lensed fiber and waveguide-input facet for our partitioned data set. For simplicity, we take the higher loss and apply it to our partitioned data set of 4-signal/4-idler channels to give a lower bound on the brightness of all photon-pair generation values. The limited angular degree of control in the setup between waveguide facet and lensed fiber is reserved for the collection-lensed fiber to ensure optimal collection of generated photon-pairs, making this additional loss likely associated with the input facet. The mean net losses per channel from waveguide to detectors range from 10.8 to 14.7 dB for 1460 to 1620 nm, with a spread in loss/channel introduced from coupling efficiency for free-space filtering and detection efficiency that both fall off outside the traditional fiber C-band (1525-1565 nm). The single photon detectors are polarization-sensitive superconducting nanowire single-photon detectors (Quantum Opus, Inc.) that have mean detection efficiencies that range between 44–73% per detector/channel as measured over a 1500 to 1620 nm span. Quantum detection efficiencies at 1470 nm were inferred from manufacturer calibration data while the value at 1490 nm is estimated from the efficiency measured at 1500 nm. The detector dark-count rates range from 110 to 130 counts/s. The detected photon counts are time stamped using a time tagger (Time Tagger 20 by Swabian

Instruments, Inc.) which allows for the singles counts and coincidence counts between detectors to be measured.

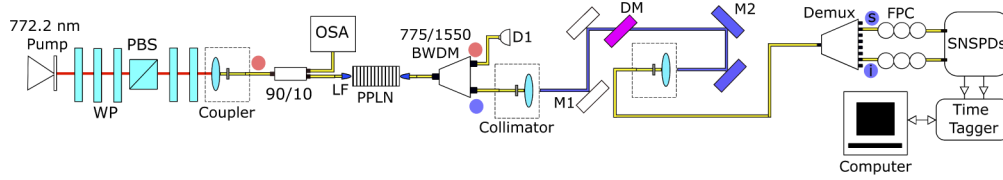


Fig. 4. Setup for correlated photon-pair generation from SPDC in a PPLN waveguide pumped with a CW pump. Red/blue lines for free space, and yellow for fiber. Before (after) waveguide fiber is single mode at 780 nm (1550 nm). LF:lensed fiber, M1, M2: broad band mirrors, DM:short-pass dichroic mirror, FPC:fiber polarization controller,D1:power meter, SNSPDs:superconducting nanowire single-photon detectors

3. Measurement of broadband-pair source

We characterize the quality of our pair source by its brightness, heralding efficiency, and coincidence-to-accidental ratio (CAR). We use a brightness metric normalized to poled waveguide-length squared (Eq. (2)), similar to what is typically used to characterize small-signal SHG conversion efficiency. Our measured (raw) normalized brightness (NB) shown in Fig. 5(a) is defined with respect to a loss-corrected pump power source (P_T) that is based on the measured pump power exiting the waveguide, but corrected for losses including fiber device loss and half the net waveguide insertion loss at the pump wavelength. In our estimated normalized brightness, we assume flat-top 18 nm channel bandwidths $\Delta\lambda_{s,i}$ for both channels of the signal-idler pair unless stated otherwise. The length L_p is defined to be the 0.03 cm total length for the poled region. Coincident count rates (CCR) are measured in pairs/s.

$$NB = \frac{CCR}{\Delta\lambda_{s,i} L_p^2 P_T} \quad (2)$$

In Fig. 5(a), we present a measured [loss-corrected] normalized brightness of $(337 \pm 6) \times 10^3$ [$(252 \pm 5) \times 10^6$] pairs/s-nm-cm²-mW at a loss-corrected pump power of -20.5 dBm for the signal-idler channels with 120 nm separation assuming 7.5 dB of facet-to-lensed fiber coupling loss stated earlier. The corresponding CAR of 6900 ± 200 in Fig. 5(b), indicates a low level of pollution from multi-photon emission and other sources of background counts. Error bars for CAR and normalized brightness are taken from the standard deviation of 10 sets of measurements each with an integration time of 60 s (total time of 600 s). For these normalized brightnesses we assume a fixed known loss and the error bars do not account for the uncertainty in measured signal/idler loss, which we estimate is ± 1 dB per channel.

Correlation counts of photon-pairs between two wide-filter channels of equal frequency bandwidth should be optimal when the frequency spacing between the signal/idler channel frequency centers f_s/f_i and half-pump frequency $f_p/2$ are equal as predicted by energy conservation in the SPDC process. Our photon-pair measurement effectively utilizes only a fraction of the channels' bandwidth because of the unequal channel-frequency bandwidths, and frequency-spacing asymmetry between f_s, f_i , and $f_p/2$. We take the loss-corrected normalized-brightness that assumes 18 nm passbands in Fig. 5(a) and replace this fixed 18 nm bandwidth of the demux filters with an effective bandwidth per channel set calculated using $f_s, f_i, f_p/2$ and the signal/idler pass-bands in Hz (illustrated in Fig. 5(c)). This bandwidth/loss-corrected normalized brightness uses frequency bandwidths that should contribute to correlation counts. The effective frequency bandwidths (1.434, 1.106, 0.909) THz are expressed with respect to the half-pump

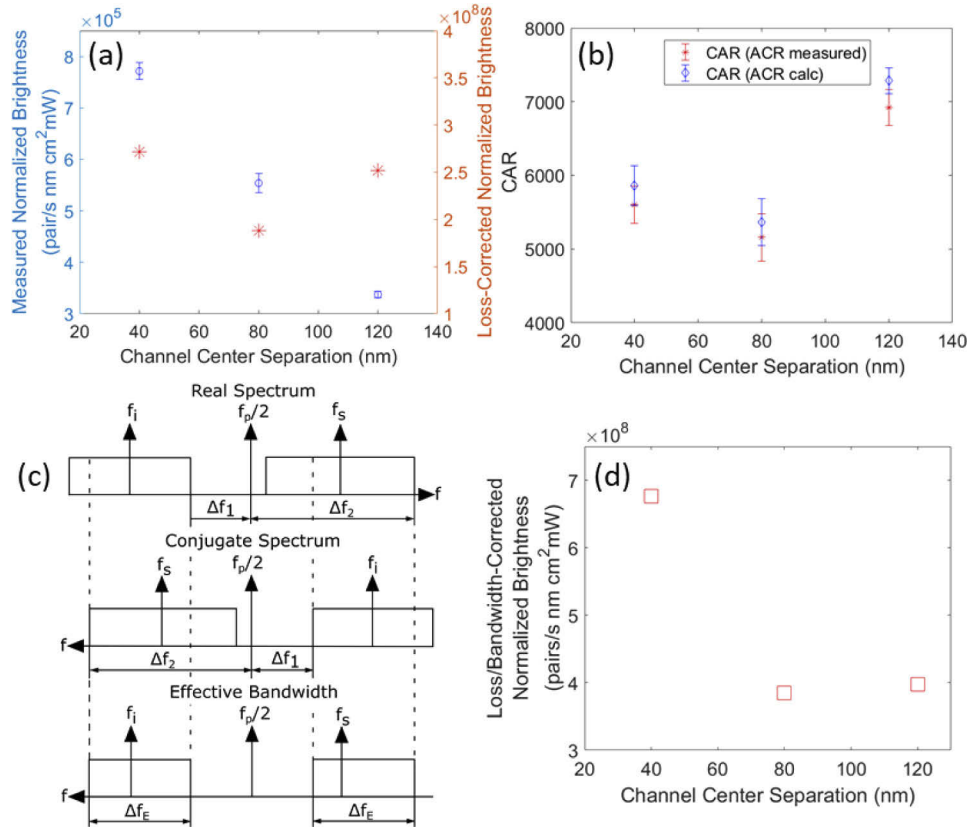


Fig. 5. (a) Mean and standard deviation of normalized brightness $\frac{\text{pairs}}{\text{s} \cdot \text{nm} \cdot \text{cm}^2 \cdot \text{mW}}$ for raw data (blue circles) and loss-corrected data (red asterisks) assuming 18 nm channel bandwidths (b) CAR and its standard deviation for 3 signal-idler channel separations. Accidental coincidence rate (ACR) is calculated using measured singles-count rates or measured directly via cross correlation of time stamps between two detection events for different channel delays. (c) Illustration of asymmetry in signal-idler channel center frequencies f_s, f_i with respect to half the pump frequency ($f_p/2$) where Δf_1 and Δf_2 define the bounds of each channel band sitting symmetric to $f_p/2$ in the real spectrum. The conjugate spectrum projects the filter boundaries and defines an effective bandwidth that should contribute to correlation counts. (d) The effective bandwidth is used per channel set in place of the 18 nm filter bandwidth to estimate the loss/bandwidth-corrected normalized brightness.

frequency ($2 \times 772.2 \text{ nm} = 1544.4 \text{ nm}$), and lead to effective bandwidths of 11.4, 8.8, and 7.2 nm for channel-sets of 1490/1610, 1510/1590, and 1530/1570 nm, respectively. The revised bandwidth/loss-corrected normalized brightness, indicated by red squares, is shown in Fig. 5(d). While we expected the pair-matching 3-dB bandwidth to far exceed 120 nm given our 15 nm SHG phase-matching bandwidth, available filters constrained the pair-generation measurement range to channels separated by 120 nm. Correcting for uncorrelated bandwidth of signal/idler filters by ratio of the design to effective bandwidth, we obtain a loss/bandwidth-corrected normalized brightness reported in Fig. 5(d) of $398 \times 10^6 \text{ pairs/s} \cdot \text{nm} \cdot \text{cm}^2 \cdot \text{mW}$. The data corrected for loss, uncorrelated-bandwidth, and length of the poled region falls in line with recent work [6] in a similar thin-film PPLN with poled region of 4 mm total length with loss-corrected normalized brightness of $431 \times 10^6 \text{ pairs/s} \cdot \text{nm} \cdot \text{cm}^2 \cdot \text{mW}$ (reported loss-corrected brightness of 69 MHz/mW/nm).

To better illustrate the impact of the half-frequency pump/channel-pair asymmetry shown in Figs. 5(a)-(d), we find all existing correlations between neighboring channel-pairs. In Fig. 6(a), we show the measured raw CCR (pairs/s) for all 16 signal-idler combinations of 4-signal and 4-idler channels. The corresponding CAR for all channel combinations is shown in Fig. 6(b). For signal-idler channel combinations where correlations are not expected nor found, the measured CCR are ≤ 0.1 pairs/s and counts are taken for total of 1 integration time $T_I = 60$ s compared to all other channel sets collected for a total of 10 integration times (600 s).

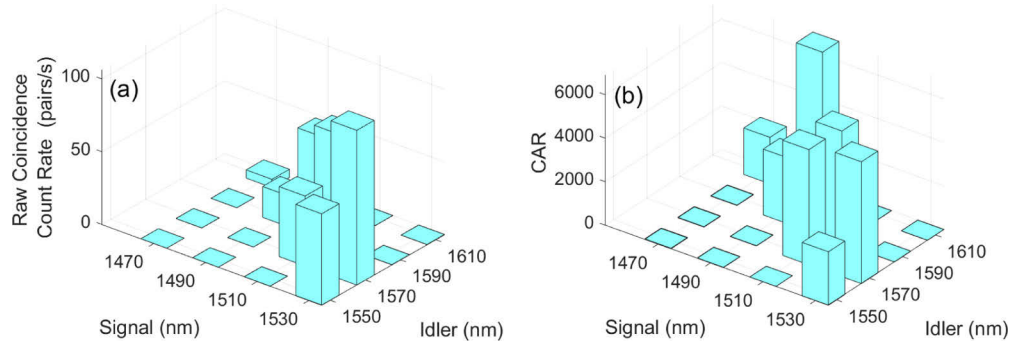


Fig. 6. (a) Photon-pair correlations expressed as coincident counts per second using asymmetric signal/idler channel-pairs of the 8-channel demux with channel-center wavelengths (1470 to 1610 nm). The pump is set at 772.2 nm on a phase matching peak around 1541 nm (771 nm SHG peak). (b) CAR measured over all channel sets in (a) uses the measured ACR

The system losses and lack of symmetry of signal-idler channels with respect to the half-frequency pump degrade the corresponding heralding efficiencies. The heralding efficiency ($HE_{T,y}$) for channel- y is defined in Eq. (3) below as the ratio of the total number of coincident counts (CC_T) to singles counts ($SC_{T,x}$) measured in channel- x where $x, y = s, i$ for signal or idler respectively. Heralding efficiencies are around 0.3 – 3 % as shown in Table 1. These heralding efficiencies are similar to other works operating under a combination of different losses, noise sources, when measuring correlated photons from waveguide sources using waveguide-fiber-coupled collection optics, and can be improved on [17]. Correcting for these wide-band channel losses and singles counts of uncorrelated bandwidth introduces significant error, for example, in 1530/1570, 1510/1590, and 1490/1610 nm channels sets we have idler heralding efficiencies of about 130, 79, and 89%, respectively. Ideally, perfectly correcting for all losses would lead to a

Table 1. Raw Heralding Efficiency ($HE_{T,y}$) measured using demux channels for signal and idler, and the associated standard deviations (STD) about their mean values

Idler (nm)	$HE_{T,i}$ (%)	\pm STD (%)	Signal (nm)	$HE_{T,s}$ (%)	\pm STD (%)
1570	1.26	0.05	1510	2.13	0.08
1550	1.17	0.04	1530	1.53	0.05
1570	1.95	0.06	1530	3.19	0.09
1590	1.83	0.08	1510	2.25	0.09
1590	1.1	0.03	1490	0.62	0.02
1610	1.54	0.03	1490	2.25	0.04
1610	0.42	0.02	1470	0.3	0.01

heralding efficiency approaching 100% for wide-band correlated-channels [18].

$$HE_{T,y} = \frac{CC_T}{SC_{T,x}} \times 100\% \quad (3)$$

4. Pair production with symmetric filtering

The results of section 3 show strong correlations despite the asymmetry of the signal/idler filters with respect to the half-frequency pump. Here we employ a programmable filter (Finisar Waveshaper 4000S) to enable symmetric filtering within the standard 1550 nm C-band using the experimental configuration depicted in Fig. 7. In order to maintain many channels in this smaller wavelength band, we program the filter bandwidth to be ≈ 6 nm. The waveshaper channel sets have C-band losses per channel of about 5 dB, and a pump isolation > 50 dB (waveshaper-input to output). From our measured losses, we infer a pump power of -20.6 dBm coming out of the waveguide (facet-to-lensed fiber coupling loss of 7.5 dB). All programmed channel sets are measured for 10 integration times (total time) of $T_I = 60$ s ($T_I = 600$ s) each with the raw values reported for CCR (pairs/s) in Fig. 8(a) and the CARs in Fig. 8(b). All errorbars are reported as the standard deviation over the set of 10 measurements (each with $T_I = 60$ s). In this setup, the correlated channels see CCR as high as 23.5 ± 0.9 pairs/s and a lower CAR (relative to Fig. 5(b)) of 36.3 ± 1.3 in channel-set 1542.0/1548.0 nm. Estimating the waveguide facet-to-lensed fiber coupling loss in the C-band as about 4.5 dB, we find loss-corrected normalized brightness of 230×10^6 , 190×10^6 , 280×10^6 pairs/s \cdot nm \cdot mW \cdot cm² in signal-idler channels of 1530.3/1560, 1536.2/1553.9, and 1542/1548 nm respectively. Total losses of ≈ 13 and 14 dB per channel that include coupling and quantum-detector losses were applied to the raw coincidence count rates along with the loss-corrected pump power and design channel bandwidth. These values are the same order-of-magnitude as both [6] and the bandwidth/loss-corrected brightnesses calculated in Fig. 5(d) where the loss-corrected normalized brightnesses should be independent of channel bandwidths, losses, pump power, and device length. In contrast, the CARs for such channel-pairs in Fig. 8(b) are much smaller than Fig. 5(b) because of extremely high levels of background counts generated inside the waveshaper in the absence of the pump. The waveshaper generates a background (pump off) singles count rate of around 2.5×10^4 cts/s per channel (irrespective of filter bandwidth) that originates from out-of-band light leakage generated inside the unit independent of any waveshaper input. This background singles count dominates the total singles count in the presence of the pump field at $\geq 92\%$ of the total counts in each channel. It increases the ACR, while reducing the CAR and the heralding efficiency. We expect this background light could be removed with appropriate filtering, but here we correct for the background light levels by appropriate subtraction techniques as described in [19] and shown in Eqs. (4)–(6).

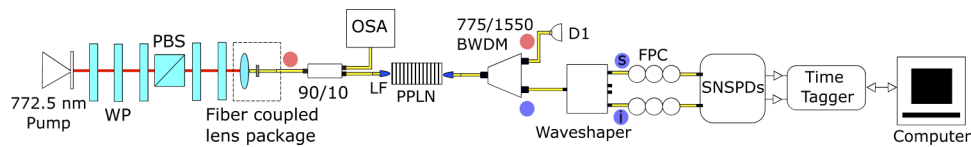


Fig. 7. Pair generation performed with computer controlled signal-idler channels of the Finisar waveshaper designed to be roughly 0.745 THz (≈ 6 nm) of passband each while the pump is centered at 772.5 nm.

We measure the background singles and accidental counts generated in the system with the pump off. We denote background singles counts in channel- x ($x=s, i$ for signal or idler) by $SC_{bkg,x}$ (pump off) that are subtracted from the total singles counts in channel- x ($SC_{T,x}$) to give the singles count due to all pump-system interactions of $SC_{T,x} - SC_{bkg,x}$. Likewise, the coincident

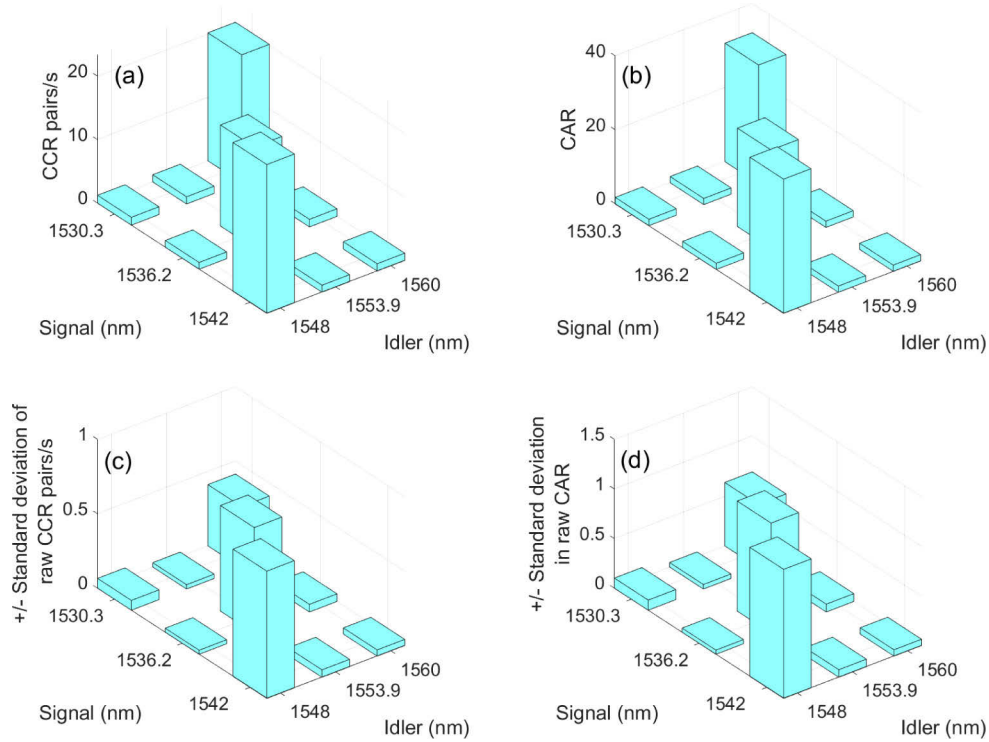


Fig. 8. (a) Mean-raw coincident-count-rate between signal-idler channel pairs using adjustable filter channels on a Finisar waveshaper (b) Corresponding mean CAR without background subtraction. (c) \pm standard deviation in CCR, (d) \pm standard deviation in CAR

counts for pump on(off) are $CC_T(CC_{bkg})$. All singles, coincident and accidental counts are measured simultaneously over the same integration time (total time) $T_I = 60$ s ($T_I = 600$ s), where coincident and accidental count events are defined for channel-delays with 1 ns time-delay bin widths T_b . The background accidental counts contributing to coincident counts are defined by CC_{bkg} in Eq. (4).

$$CC_{bkg} = (SC_{T,s} \cdot SC_{bkg,i} + SC_{bkg,s} \cdot SC_{T,i} - SC_{bkg,s} \cdot SC_{bkg,i}) \cdot T_b / T_I \quad (4)$$

The background-corrected heralding efficiencies $HE_{c,y}$ and their standard deviations for $y, x = s, i$, for the signal and idler are calculated from Eq. (5), are shown in Table 2.

$$HE_{c,y} = \frac{CC_T - CC_{bkg}}{SC_{T,x} - SC_{bkg,x}} \times 100\% \quad (5)$$

The raw CARs in correlated channels shown in Fig. 8(b) of order 10 increase by nearly 3 orders of magnitude after background subtraction (Eq. (6)), exceeding CAR levels in Fig. 5(b). For the 1530.3-1560.0 nm channel-pair, the raw CAR of 32.1 ± 0.6 becomes $152 \pm 9 \times 10^2$ after background subtraction. The background-corrected CAR uses an accidental count inferred from the singles counts of $AC_T = SC_{T,i} \cdot SC_{T,s} \cdot T_b / T_I$ in place of the AC_T found directly in the cross-correlation measurement, and shows no significant difference in value.

$$CAR_c = \frac{CC_T - CC_{bkg}}{AC_T - CC_{bkg}} \quad (6)$$

Comparing Fig. (8) to Fig. (6) we see that symmetric filtering makes the correlation matrix a clean diagonal in contrast to Fig. 6(a).

Table 2. Mean heralding efficiency ($HE_{c,y}$) with background (pump off) subtraction for signal-idler channel pairs that are symmetric with respect to half the pump frequency. The error about the mean values are expressed as the standard deviation (STD).

Idler (nm)	$HE_{c,i}$ (%)	\pm STD (%)	Signal (nm)	$HE_{c,s}$ (%)	\pm STD (%)
1548.0	1.07	0.04	1542.0	2.49	0.12
1554.0	0.93	0.05	1536.2	2.27	0.15
1560.0	0.94	0.03	1530.3	3.15	0.15

5. Conclusion

We have successfully demonstrated correlated-pair measurements on a 300-um long poled-region of lithium-niobate on-insulator platform with a signal-idler channel separations exceeding 120 nm. The large bandwidth was segmented using standard filtering technology, including demonstrating correlations on several channels of the demux CWDM grid. This technology has the potential to serve as chip-based sources of entangled pairs where the broad and continuous pair-matching signal-idler channel-bandwidths offer high channel capacities for a large number of users. The lack of noise processes from fluorescence of the pump allows the SPDC process to occur with high CARs. In the future, low-loss coupling [20] and filtering can lead to much higher heralding efficiencies than the 3 % measured here. Correcting for all losses from waveguide to detectors would bring the heralding efficiency of the 1490/1610 demux channels to 90% and 73% respectively. Elimination of some fraction of this loss would make this type of waveguide technology a good choice for entangled pair generation in quantum photonic integrated circuits, including for wavelength division multiplexed systems.

Funding

Office of Naval Research (N000141712409).

Acknowledgments

The authors would like to thank Drs. Aaron Miller and Timothy Rambo at Quantum Opus for their assistance with the Opus One superconducting nanowire single-photon detectors. We would also like to thank Dr. Michael Schlagmüller at Swabian Instruments for discussions relating to the Time Tagger 20.

Disclosures

The authors declare that there are no conflicts of interest related to this article.

References

1. A. Rao and S. Fathpour, "Heterogeneous thin-film lithium niobate integrated photonics for electrooptics and nonlinear optics," *IEEE J. Sel. Top. Quantum Electron.* **24**(6), 1–12 (2018).
2. R. Luo, Y. He, H. Liang, M. Li, and Q. Lin, "Highly tunable efficient second-harmonic generation in a lithium niobate nanophotonic waveguide," *Optica* **5**(8), 1006–1011 (2018).
3. M. Jin, J.-Y. Chen, Y. M. Sua, and Y.-P. Huang, "High-extinction electro-optic modulation on lithium niobate thin film," *Opt. Lett.* **44**(5), 1265–1268 (2019).
4. H. Jin, F. M. Liu, P. Xu, J. L. Xia, M. L. Zhong, Y. Yuan, J. W. Zhou, Y. X. Gong, W. Wang, and S. N. Zhu, "On-chip generation and manipulation of entangled photons based on reconfigurable lithium-niobate waveguide circuits," *Phys. Rev. Lett.* **113**(10), 103601 (2014).
5. C. Wang, C. Langrock, A. Marandi, M. Jankowski, M. Zhang, B. Desiatov, M. M. Fejer, and M. Lončar, "Ultrahigh-efficiency wavelength conversion in nanophotonic periodically poled lithium niobate waveguides," *Optica* **5**(11), 1438–1441 (2018).
6. J. yang Chen, Y. M. Sua, Z. hui Ma, C. Tang, Z. Li, and Y. ping Huang, "Efficient parametric frequency conversion in lithium niobate nanophotonic chips," *OSA Continuum* **2**(10), 2914–2924 (2019).

7. A. Rao, K. Abdelsalam, T. Sjaardema, G. F. Camacho-González, A. Honardoost, and S. Fathpour, "Highly efficient nonlinear integrated photonics in ultracompact periodically-poled lithium niobate on silicon," in *Frontiers in Optics / Laser Science*, (Optical Society of America, 2018), p. JTU3A.59.
8. A. Rao, K. Abdelsalam, T. Sjaardema, A. Honardoost, G. F. Camacho-Gonzalez, and S. Fathpour, "Actively-monitored periodic-poling in thin-film lithium niobate photonic waveguides with ultrahigh nonlinear conversion efficiency of 4600 %/W.cm²," *Opt. Express* **27**(18), 25920–25930 (2019).
9. K. R. Parameswaran, R. K. Route, J. R. Kurz, R. V. Roussev, M. M. Fejer, and M. Fujimura, "Highly efficient second-harmonic generation in buried waveguides formed by annealed and reverse proton exchange in periodically poled lithium niobate," *Opt. Lett.* **27**(3), 179–181 (2002).
10. A. Rao, N. Nader, M. J. Stevens, T. Gerrits, O. S. Magaña-Loaiza, G. F. Camacho-González, J. Chiles, A. Honardoost, M. Malinowski, R. Mirin, and S. Fathpour, "Photon pair generation on a silicon chip using nanophotonic periodically-poled lithium niobate waveguides," in *2018 Conference on Lasers and Electro-Optics (CLEO)*, (2018) pp. 1–2.
11. C. Chen, A. Riazi, E. Y. Zhu, M. Ng, A. V. Gladyshev, P. G. Kazansky, and L. Qian, "Turn-key diode-pumped all-fiber broadband polarization-entangled photon source," *OSA Continuum* **1**(3), 981–986 (2018).
12. F. Samara, A. Martin, C. Autebert, M. Karpov, T. J. Kippenberg, H. Zbinden, and R. Thew, "High-rate photon pairs and sequential time-bin entanglement with si₃n₄ microring resonators," *Opt. Express* **27**(14), 19309–19318 (2019).
13. R. Luo, H. Jiang, S. Rogers, H. Liang, Y. He, and Q. Lin, "On-chip second-harmonic generation and broadband parametric down-conversion in a lithium niobate microresonator," *Opt. Express* **25**(20), 24531–24539 (2017).
14. B. S. Elkus, K. Abdelsalam, A. Rao, V. Velev, S. Fathpour, P. Kumar, and G. S. Kanter, "Generation of correlated photon-pairs in short thin-film lithium-niobate waveguides," in *Frontiers in Optics + Laser Science APS/DLS*, (Optical Society of America, 2019), p. LTu1D.3.
15. M. Fiorentino, S. M. Spillane, R. G. Beausoleil, T. D. Roberts, P. Battle, and M. W. Munro, "Spontaneous parametric down-conversion in periodically poled ktp waveguides and bulk crystals," *Opt. Express* **15**(12), 7479–7488 (2007).
16. R. W. Boyd, *Nonlinear optics* (Academic Press, Burlington, MA, 2008), 3rd ed.
17. N. Montaut, L. Sansoni, E. Meyer-Scott, R. Ricken, V. Quiring, H. Herrmann, and C. Silberhorn, "High-efficiency plug-and-play source of heralded single photons," *Phys. Rev. Appl.* **8**(2), 024021 (2017).
18. E. Meyer-Scott, N. Montaut, J. Tiedau, L. Sansoni, H. Herrmann, T. J. Bartley, and C. Silberhorn, "Limits on the heralding efficiencies and spectral purities of spectrally filtered single photons from photon-pair sources," *Phys. Rev. A* **95**(6), 061803 (2017).
19. S. X. Wang and G. S. Kanter, "Robust multiwavelength all-fiber source of polarization-entangled photons with built-in analyzer alignment signal," *IEEE J. Sel. Top. Quantum Electron.* **15**(6), 1733–1740 (2009).
20. L. He, M. Zhang, A. Shams-Ansari, R. Zhu, C. Wang, and L. Marko, "Low-loss fiber-to-chip interface for lithium niobate photonic integrated circuits," *Opt. Lett.* **44**(9), 2314–2317 (2019).